Jour. of the KGS Vol. 17, No. 3. June 2001, pp 25~32

A Smooth Elasto-Plastic Cap Model(II): Integration Algorithm and Tangent Operator

연속 탄소성 캡 모델(II):응력적분 및 접선계수

Seo, Young-Kyo* 서 영 교

요 지

보편적인 탄소성 캡 모델은 전통적인 등방 이론에 기초를 두고 있다. 이러한 모델의 응력적분 및 접선 계수의 유도는 여러 가지 논문들에 나타나 있지만 축차 및 체적 거동을 동시에 다루는 내제적인 해석법을 통한 지반해석은 아직까지는 많은 도전이 요구되고 있다. 앞선 동반 논문에서는 비연속적으로 연결된 항복면 사이의 접선 계수는 특이점이 됨을 나타내었고 이에 대하여 새로운 캡 모델의 구성식이 제시되었다. 본 논문에서는 제시된 캡 모델의 비 조건적이고 안정된 내재적 응력적분 및 일관된 탄소성 접선계수를 유도하였다. 또한 간단한 예제들 통하여 모델의 수행능력을 보여주었고 사면안정계산이 수행되었다.

Abstract

The widely used elasto-plastic cap models are based on the classical isotropic theory. While numerical integration algorithms and tangent operators for these models have been presented in the literature, performing implicit analysis of earthen systems using cap models remains a challenging endeavor. It was shown in the companion paper that the elasto-plastic tangent operators at the corner points on such yield surfaces were singular, giving rise to the potential numerical difficulties. To avoid such difficulties associated with corner regions, a novel, three-surface elasto-plastic cap model in which the three surfaces intersect smoothly was developed. In this paper, an unconditional stable integration algorithm and expression for consistent tangent operators are presented. Sample computations demonstrating good performance of the model on the simple material test and the slope stability analysis are presented.

Keywords : Cap models, Elasto-Plasticity, Finite element method, Soil Models, Computational Plasticity

1. Introduction

In recent years, a number of computational geomechanical models have been proposed. The most popular and widely used models are cap models advanced by DiMaggio and Sandler(1971). These cap models are based on classical isotropic elasto-plasticity theory, and couple the Drucker-Prager failure envelope with a hardening compression cap surface. In cap models, the hardening cap is an elliptical surface with a constant ratio of major to minor radius, and it intersects the failure envelope in a non-smooth fashion.

In companion paper, this non-smooth cap model was briefly introduced, and the difficulty with singular tangent operator at the corner regions was highlighted first. Then, a novel smooth cap model was presented

* Member, Fulltime Researcher, Pusan National Univ.

along with the active yield surface determination for the plastic correction. In this paper, a detailed integration algorithm and expressions for consistent tangent operators are presented for the completeness of the model. The integration algorithm presented is based on the Backward Euler integration of the rate constitutive equations which give rise to an elasto-predictor, plastic-corrector stress update algorithm. Differentiation of the incremental stress update algorithms provides expressions for the so-called consistent tangent operators which facilitate good convergence characteristics in implicit structural analysis of soil structures. In the sample computations, the excellent performance of the model is first demonstrated on a number of simple material test type computations, and then on full scale slope stability problem.

2. Stress Updates Algorithms

2.1 Case 1 Integration Algorithm

When the elastic trial state leads to $(f_1)^{tr}_{n+1} > \mathrm{TOL}_1$, the trial stress point σ^{tr}_{n+1} returns to the surface $f_1 = 0$ via a plastic correction. By integration of the associated flow rule with the Backward Euler integration algorithm, the plastic strain increment for Case 1 is computed as

$$\triangle \varepsilon^{p}_{n+1} = \hat{\gamma}^{1}_{n+1}\left(\frac{\partial f_1}{\partial \sigma}\right)_{n+1} = \hat{\gamma}^{1}_{n+1}(n - F_e^{'}\,1)_{n+1} \qquad (1)$$

where $F_e^{'}$ is the partial derivative of F_e with respect to I_1. Using the Backward Euler integration rule which gives rise to plastic-correction of the elastic prediction, the updated stress can thus be written as

$$\begin{aligned}\sigma_{n+1} &= \sigma^{tr}_{n+1} - C : \triangle \varepsilon^{p}_{n+1} \\ &= \sigma^{tr}_{n+1} - 2\mu \hat{\gamma}^{1}_{n+1} n_{n+1} + 3K \hat{\gamma}^{1}_{n+1} F_e^{'}\,1 \end{aligned} \qquad (2)$$

and similarly the updated back stress is obtained as

$$q_{n+1} = q_n + H \hat{\gamma}^{1}_{n+1} n_{n+1} \qquad (3)$$

The diviatoric and trace portions of the updated stress can be written as

$$s_{n+1} = s^{tr}_{n+1} - 2\mu \hat{\gamma}^{1}_{n+1} n_{n+1} \qquad (4a)$$

$$(I_1)_{n+1} = (I_1)^{tr}_{n+1} + 9K \hat{\gamma}^{1}_{n+1} F_e^{'}(I_1) \qquad (4b)$$

To complete the stress update, the plasticity consistency parameter $\hat{\gamma}^{1}_{n+1}$ is computed directly such that the stresses lie on the Drucker-Prager surface $f_1 = 0$. The expression is as follows

$$\hat{\gamma}^{1}_{n+1} = \frac{(f_1)^{tr}_{n+1}}{2\mu + 9K(F_e^{'})^2} \qquad (5)$$

Once $\hat{\gamma}^{1}_{n+1}$ is computed and the stresses have been updated, then the compression cap parameter can be updated by the nonlinear equation

$$x_{n+1} = x_n + h^{'}(x_{n+1})\ tr(\triangle \varepsilon^{p}_{n+1}) \qquad (6)$$

which must be performed iteratively since $h^{'}$ depends upon the updated value of x_{n+1}.

2.2 Case 2 Integration Algorithm

When the compression cap surface is active, then the elastic stress predictor must return to the compression cap surface, which will generally translate and grow/ shrink during the return map process. (Note: If the portion of the compression cap surface lying between x and $I_1^C(x)$ is active, then the compression cap surface will actually be moving inward on the I_1 axis with a decreasing radius, where as if the portion lying between x and $X(x)$ is active, the surface translates outward on the I_1 axis with an increasing radius $R(x)$.)

Backward Euler integration of the Case 2 associated flow rule gives a plastic strain increment as follows

$$\triangle \varepsilon^{p}_{n+1} = \hat{\gamma}^{2}_{n+1}\left(\frac{\partial f_2}{\partial \sigma}\right)_{n+1} = \hat{\gamma}^{2}_{n+1}\left(2\eta - \frac{\partial F_c}{\partial I_1}1\right)_{n+1} \qquad (7)$$

resulting in the following stress update equation

$$\sigma_{n+1} = \sigma^{tr}_{n+1} + 3K \hat{\gamma}^{2}_{n+1} 1 \left(\frac{\partial F_c}{\partial I_1}\right)_{n+1} - 4\mu \hat{\gamma}^{2}_{n+1} \eta_{n+1} \qquad (8)$$

Decomposing the updated stress into its deviatoric and bulk components provides

$$s_{n+1} = s^{tr}_{n+1} - 4\mu\,\hat{\gamma}^2_{n+1}\eta_{n+1} \tag{9a}$$

$$(I_1)_{n+1} = (I_1)^{tr}_{n+1} + 9K\hat{\gamma}^2_{n+1}\left(\frac{\partial F_c}{\partial I_1}\right)_{n+1} \tag{9b}$$

Similarly, the compression cap parameter x and the back stress q have updates of the form

$$x_{n+1} = x_n - 3h'(x_{n+1})\hat{\gamma}^2_{n+1}\left(\frac{\partial F_c}{\partial I_1}\right)_{n+1} \tag{10a}$$

$$q_{n+1} = q_n + 2H\hat{\gamma}^2_{n+1}\eta_{n+1} \tag{10b}$$

The objective of the plastic correction stress update algorithm for Case 2 is thus to solve the value of the generalized plastic consistency parameter $\hat{\gamma}^2_{n+1}$ as well as I_1 and x, which satisfy Equations (9b) and (10a) and the plastic consistency condition, namely

$$(f_2)_{n+1} = \frac{||\eta^{tr}_{n+1}||^2}{\left[1+2(2\mu+H)\,\hat{\gamma}^2_{n+1}\right]^2} - F_c(I_{1_{n+1}}, x_{n+1}) = 0 \tag{11}$$

Hence the Case 2 return map involves solving a system of three highly nonlinear Equations (9b, 10a, 11) for the three coupled parameters $\hat{\gamma}^2_{n+1}$, $(I_1)_{n+1}$ and x_{n+1}. So that a solution to this system of equations can be reliably obtained, a robust and fully implicit algorithm is developed below.

Since a sequential linearization algorithm is used to solve the system, the total derivative of f_2 with respect to $\hat{\gamma}^2_{n+1}$ is needed, and is thus computed as

$$\frac{df_2}{d\hat{\gamma}^2_{n+1}} = \frac{d||\eta_{n+1}||^2}{d\hat{\gamma}^2_{n+1}} - \left(\frac{\partial F_c}{\partial I_1}\right)\frac{dI_1}{d\hat{\gamma}^2_{n+1}} - \left(\frac{\partial F_c}{\partial x}\right)\frac{dx}{d\hat{\gamma}^2_{n+1}} \tag{12}$$

Since the derivatives of $(I_1)_{n+1}$ and x_{n+1} are coupled, they must be written as follows

$$\begin{bmatrix} A_{11} & A_{12} \\ A_{21} & A_{22} \end{bmatrix}\begin{bmatrix} \dfrac{dI_1}{d\hat{\gamma}^2_{n+1}} \\ \dfrac{dx}{d\hat{\gamma}^2_{n+1}} \end{bmatrix} = \begin{bmatrix} F_1 \\ F_2 \end{bmatrix} \tag{13}$$

where

$$A = \begin{bmatrix} 1 - 9K\hat{\gamma}^2_{n+1}\left(\dfrac{\partial^2 F_c}{\partial I_1^2}\right) & -9K\hat{\gamma}^2_{n+1}\left(\dfrac{\partial^2 F_c}{\partial I_1 \partial x}\right) \\ 3h'\hat{\gamma}^2_{n+1}\left(\dfrac{\partial^2 F_c}{\partial I_1^2}\right) & 1 + 3\hat{\gamma}^2_{n+1}\left[h''\left(\dfrac{\partial F_c}{\partial I_1}\right) + h'\left(\dfrac{\partial^2 F_c}{\partial I_1 \partial x}\right)\right] \end{bmatrix} \tag{14a}$$

$$F = \begin{bmatrix} 9K\left(\dfrac{\partial F_c}{\partial I_1}\right) \\ -3h'\left(\dfrac{\partial F_c}{\partial I_1}\right) \end{bmatrix} \tag{14b}$$

Utilizing Cramer's Rule, the desired derivatives can be straightforwardly obtained as follows

Table 1. Fully implicit return map algorithm for Case 2

$k = 0$

$(I_1)^k_{n+1} = (I_1)^{tr}_{n+1}$; $x^k_{n+1} = x^{tr}_{n+1}$; $\eta^k_{n+1} = \eta^{tr}_{n+1}$

compute $(f_2)^k_{n+1} = f_2(\eta^{tr}_{n+1}, (I_1)^{tr}_{n+1}, x^{tr}_{n+1})$

while ($(f_2)^k_{n+1} >$ TOL$_2$) **then**

compute $\left(\dfrac{df_2}{d\hat{\gamma}^2}\right)^{k+1}_{n+1}$ by equations (12), (15)

$(\hat{\gamma}^2)^{k+1}_{n+1} = (\hat{\gamma}^2)^k_{n+1} - \left(f_2\left[\dfrac{df_2}{d\hat{\gamma}^2}\right]^{-1}\right)^k_{n+1}$

Iteratively update $(I_1)^{k+1}_{n+1}$ and x^{k+1}_{n+1} (see Table 2)

Compute $(f_2)^{k+1}_{n+1}$ by Equation (11)

$k = k+1$

End while

Given $\hat{\gamma}^2_{n+1}$; $(I_1)_{n+1}$; x_{n+1}, update stresses and compute tangent operator

return

Table 2. Algorithm for simultaneous update of I_1 and x for Case 2

For notational simlicity, let $x_1 = I_1$ and $x_2 = x$

$j = 0$

let $x_1^j = (I_1)_{n+1}^j$ and $x_2^j = x_{n+1}^j$ assume prior values (see Table 1)

compute $r(x^j)$ by Equation (16)

While ($||r(x^j)||$ > TOL) **then**

$$x^{j+1} = x^j - \left(\frac{dr}{dx}\right)_j^{-1} \cdot r_j$$

update $r(x^{j+1})$ by Equation (16)

$j = j+1$

End while

$$\frac{dI_1}{d\hat{\gamma}_{n+1}^2} = \frac{F_1 A_{22} - F_2 A_{12}}{A_{11}A_{22} - A_{12}A_{21}} \tag{15a}$$

$$\frac{dx}{d\hat{\gamma}_{n+1}^2} = \frac{F_2 A_{11} - F_1 A_{21}}{A_{11}A_{22} - A_{12}A_{21}} \tag{15b}$$

With all the preceding derivatives in hand, the fully implicit closest point projection algorithm for determination of $\hat{\gamma}_{n+1}^2$ is shown in Table 1.

Once a trial value of $\hat{\gamma}_{n+1}^2$ is obtained (in the algorithm of Table 1), then I_1 and x must be updated. Due to the nonlinearity of the updated Equations (9b) and (10a), the update of I_1 and x is nontrivial, even with a fixed value of $\hat{\gamma}_{n+1}^2$. Defining a residual vector based on Equations (9b) and (10a) as follows,

$$r(I_1, x) = \begin{bmatrix} (I_1)_{n+1} - (I_1)_{n+1}^{tr} - 9K\hat{\gamma}_{n+1}^2 \left(\frac{\partial F_c}{\partial I_1}\right) \\ x - x_n + 3h'(x_n+1)\hat{\gamma}_{n+1}^2 \left(\frac{\partial F_c}{\partial I_1}\right) \end{bmatrix} \tag{16}$$

a Newton's method based on iterative linerization of the residual function is presented in Table 2 for updating I_1 and x.

2.3 Case 3 Integration Algorithm

When the Case 3 is active, or when the return point for Case 2 lies in the domain of the tension cap, then the stress must return to the tension cap surface. Since the tension cap has a fixed radius, the Case 3 return mapping algorithm is considerably simpler than that for the compression cap.

Integration of the associated Case 3 flow rule gives the following plastic strain increment,

$$\triangle \varepsilon_{n+1}^p = \hat{\gamma}_{n+1}^3 \left(\frac{\partial f_3}{\partial \sigma}\right)_{n+1} = \hat{\gamma}_{n+1}^3 \left(2\eta - \frac{\partial F_t}{\partial I_1} 1\right)_{n+1} \tag{17}$$

and the corrected stress and back stress can be written as

$$\sigma_{n+1} = \sigma_{n+1}^{tr} + 3K\hat{\gamma}_{n+1}^3 1 \left(\frac{\partial F_t}{\partial I_1}\right)_{n+1} - 4\mu\hat{\gamma}_{n+1}^3 \eta_{n+1} \tag{18a}$$

$$q_{n+1} = q_n + 2H\hat{\gamma}_{n+1}^3 \eta_{n+1} \tag{18b}$$

Decomposition of the corrected stresses and back stresses into deviatoric and bulk components gives

$$s_{n+1} = s_{n+1}^{tr} - 4\mu\hat{\gamma}_{n+1}^3 \eta_{n+1} \tag{19a}$$

$$\begin{aligned} (I_1)_{n+1} &= (I_1)_{n+1}^{tr} + 9K\hat{\gamma}_{n+1}^3 \left(\frac{\partial F_t}{\partial I_1}\right)_{n+1} \\ &= (I_1)_{n+1}^{tr} - 18K\hat{\gamma}_{n+1}^3 (I_1)_{n+1} \end{aligned} \tag{19b}$$

The remaining objective of the return map algorithm is to enforce the plastic consistency condition

$$(f_3)_{n+1} = \frac{||\eta_{n+1}^{tr}||^2}{\left[1 + 2(2\mu + H)\hat{\gamma}_{n+1}^3\right]^2} - F_t(I_1)_{n+1} = 0 \tag{20}$$

The return map algorithm for Case 3 is necessarily iterative, and the Newton's method algorithm of Table 3 is very efficient and robust. Once the Case 3 return map is successfully completes, the compression cap parameter x is updated iteratively following Equation (6).

Table 3. Return map algorithm for Case 3

$k=0$

$(I_1)^k_{n+1}=(I_1)^{tr}_{n+1};\ \eta^k_{n+1}=\eta^{tr}_{n+1}$

compute $(f_3)^k_{n+1}=(f_3)^{tr}_{n+1}=f_3(\eta^{tr}_{n+1},(I_1)^{tr}_{n+1})$

While ($(f_3)^k_{n+1} > \mathrm{TOL}_3$) **then**

compute $\left(\frac{df_3}{d\hat{\gamma}^3}\right)^k_{n+1}=\left[\frac{-4(2\mu+H)\|\eta\|^2}{(1+2(2\mu+H)\hat{\gamma}^3)^2}-\frac{9K(F_t')^2}{1-9KF_t''\hat{\gamma}^3}\right]^k_{n+1}$

$(\hat{\gamma}^3)^{k+1}_{n+1}=(\hat{\gamma}^3)^k_{n+1}-\left(f_3\left(\frac{df_3}{d\hat{\gamma}^3}\right)^{-1}\right)^k_{n+1}$

update $(I_1)^{k+1}_{n+1}$ by Equation (19b)

compute $(f_3)^{k+1}_{n+1}$ by Equation (20)

$k=k+1$

End while

Perform update final update of σ_{n+1}, q_{n+1}, x_{n+1} and compute tangent operator

return

3. Consistent Tangent Operators

In modern computational plasticity, it is now recognized (Simo and Taylor, 1985) that in order to achieve the asymptotically quadratic rate of force-balance convergence that is theoretically possible with global Newton-Raphson force balance iterations, material tangent operators that are consistent with the implemented (discrete) form of the constitutive models must be utilized. The consistent tangent operators are defined as

$$C^{cons}_{n+1}=\frac{\partial\triangle\sigma_{n+1}}{\partial\triangle\varepsilon_{n+1}} \tag{21}$$

Since the derivation of expressions for consistent tangent operators is conceptually straightforward(Simo and Taylor, 1985), albeit algebraically complex, expressions for the consistent tangent operators for the three subcases of the smooth cap model are presented in the following sub-sections.

3.1 Case 1: Consistent Tangent Operator

The symmetrical Case 1 consistent tangent operator is computed as follows

$$C^{cons}_{n+1}=C^{elastic}-\frac{\left[2\mu n_{n+1}-\left(\frac{3KF_e'}{1-9K\hat{\gamma}^1_{n+1}F_e''}\right)1\right]\otimes\left[2\mu n_{n+1}-\left(\frac{3KF_e'}{1-9K\hat{\gamma}^1_{n+1}F_e''}\right)1\right]}{(2\mu+H)+\frac{9K(F_e')^2}{1-9K\hat{\gamma}^1_{n+1}F_e''}}+\frac{9K^2\hat{\gamma}^1_{n+1}F_e''}{1-9K\hat{\gamma}^1_{n+1}F_e''}1\otimes1-\frac{4\mu^2\hat{\gamma}^1_{n+1}}{\|\eta^{tr}_{n+1}\|}[I_{dev}-n_{n+1}\otimes n_{n+1}] \tag{22}$$

3.2 Case 2: Consistent Tangent Operator

The Case 2 consistent tangent operator is computed as follows

$$C^{cons}_{n+1}=C^{elastic}-A_5(1\otimes\eta_{n+1})-A_6(\eta_{n+1}\otimes1)+A_7(1\otimes1)-A_8(\eta_{n+1}\otimes\eta_{n+1})-A_9I_{dev} \tag{23}$$

where

$$A_1=1-9K\hat{\gamma}^2_{n+1}\left(\frac{\partial^2F_c}{\partial I_1^2}\right)+\frac{27Kh'(\hat{\gamma}^2_{n+1})^2\left(\frac{\partial^2F_c}{\partial I_1^2}\right)\left(\frac{\partial^2F_c}{\partial I_1\partial x}\right)}{1+3\hat{\gamma}^2_{n+1}\left[h''\left(\frac{\partial F_c}{\partial I_1}\right)+h'\left(\frac{\partial^2F_c}{\partial I_1\partial x}\right)\right]} \tag{24a}$$

$$A_2=\frac{-3\hat{\gamma}^2_{n+1}h'\left(\frac{\partial^2F_c}{\partial I_1^2}\right)}{1+3\hat{\gamma}^2_{n+1}\left[h''\left(\frac{\partial F_c}{\partial I_1}\right)+h'\left(\frac{\partial^2F_c}{\partial I_1\partial x}\right)\right]} \tag{24b}$$

$$A_3 = \frac{\left(\frac{\partial^2 F_c}{\partial I_1^2}\right) + A_2\left(\frac{\partial^2 F_c}{\partial I_1 \partial x}\right)}{A_1} \tag{24c}$$

$$A_4 = \left(\frac{\partial^2 F_c}{\partial I_1^2}\right)\frac{dI_1}{d\hat{\gamma}^2_{n+1}} + \left(\frac{\partial^2 F_c}{\partial I_1 \partial x}\right)\frac{dx}{d\hat{\gamma}^2_{n+1}} \tag{24d}$$

$$A_5 = \frac{12K\mu}{[1+2(2\mu+H)\hat{\gamma}^2_{n+1}]\frac{df_2}{d\hat{\gamma}^2_{n+1}}}\left[\left(\frac{\partial F_c}{\partial I_1}\right) + A_4\hat{\gamma}^2_{n+1}\right] \tag{24e}$$

$$A_6 = \frac{12K\mu}{[1+2(2\mu+H)\hat{\gamma}^2_{n+1}]\frac{df_2}{d\hat{\gamma}^2_{n+1}}}\left[\left(\frac{\partial F_c}{\partial I_1}\right)\frac{1}{A_1} + \frac{A_2}{A_1}\left(\frac{\partial F_c}{\partial x}\right)\right] \tag{24f}$$

$$A_7 = 9K^2\left[A_3\hat{\gamma}^2_{n+1} + \frac{\left[\left(\frac{\partial F_c}{\partial I_1}\right) + A_4\hat{\gamma}^2_{n+1}\right]\left[\left(\frac{\partial F_c}{\partial I_1}\right)\frac{1}{A_1} + \frac{A_2}{A_1}\left(\frac{\partial F_c}{\partial x}\right)\right]}{\frac{df_2}{d\hat{\gamma}^2_{n+1}}}\right] \tag{24g}$$

$$A_8 = \frac{16\mu^2}{\frac{df_2}{d\hat{\gamma}^2_{n+1}}}\left[\frac{1 + 4(2\mu+H)\hat{\gamma}^2_{n+1}}{[1+2(2\mu+H)\hat{\gamma}^2_{n+1}]^2}\right] \tag{24h}$$

$$A_9 = \frac{8\mu^2\hat{\gamma}^2_{n+1}}{1+2(2\mu+H)\hat{\gamma}^2_{n+1}} \tag{24i}$$

Inspection of the above consistent operator proves to be non-symmetrical arising from the terms with coefficients A_5 and A_6. This is to be expected, since the hardening law governing the cap parameter x is non-associated, and the Principle of Maximum Plastic Dissipation guarantees a symmetric consistent tangent only for associated flow rules and associated hardening laws. Hofstetter et al(1993) developed an associated hardening law for the cap parameter x, and found that this did indeed lead to a symmetrical expression for the Case 2 consistent tangent operator. However, implementing an associated hardening law for x changes the mechanical response characteristics of the model. Specifically, in the implementation presented in Hofstetter et al(1993), the Drucker-Prager envelope and the tension cap yield functions were not expressed as function of x, and consequently, loading on these yield surfaces, which results in plastic dilatance, does not lead to the usual retraction of the cap. For this reason, the associated hardening law proposed in Hofstetter et al(1993) has not been adopted here.

The consistent tangent operator expression above can be symmetrized and utilized. While the symmetrized consistent tangent operator is not precisely consistent with the Case 2 integration algorithm, it still gives much better performance in nonlinear finite computations than the classical elasto-plastic continuum tangent operator. It is proposed here that the consistent tangent operator be symmetrized as follows

$$C^{symm}_{n+1} = \frac{1}{2}\left[C^{cons}_{n+1} + (C^{cons}_{n+1})^T\right] \tag{25}$$

3.3 Case 3: Consistent Tangent Operator

The symmetrical Case 3 consistent tangent operator is computed as follows

$$C^{cons}_{n+1} = C^{elastic} - \frac{8\mu^2\hat{\gamma}^3_{n+1}}{1+2(2\mu+H)\hat{\gamma}^3_{n+1}} I_{dev} + \frac{9K^2F_t''\hat{\gamma}^3_{n+1}}{1-9KF_t'\mu^2\hat{\gamma}^3_{n+1}} 1\otimes 1 - \frac{\left[\left(\frac{4\mu}{1+2(2\mu+H)\hat{\gamma}_{n+1^3}}\right)\eta_{n+1} - \left(\frac{3KF_t'}{1-9KF_t'\hat{\gamma}_{n+1^3}}\right)1\right]}{\frac{4\|\eta_{n+1}\|^2(2\mu+H)}{1+2(2\mu+H)\hat{\gamma}^3_{n+1}} + \frac{9K(F_t')^2}{1-9KF_t''\hat{\gamma}^3_{n+1}}} \otimes \frac{\left[\left(\frac{4\mu}{1+2(2\mu+H)\hat{\gamma}^3_{n+1}}\right)\eta_{n+1} - \left(\frac{3KF_t'}{1-9KF_t''\hat{\gamma}^3_{n+1}}\right)1\right]}{\frac{4\|\eta_{n+1}\|^2(2\mu+H)}{1+2(2\mu+H)\hat{\gamma}^3_{n+1}} + \frac{9K(F_t')^2}{1-9KF_t''\hat{\gamma}^3_{n+1}}} \tag{26}$$

4. Example Computations

4.1 Hydrostatic Compression Test

This simple test is designed to show the pressure versus volumetric strain behavior of the smooth cap

Table 4. Material parameters used in hydrostatic compression test

Material Parameter	value
μ	170.0 MPa
K	210.0 MPa
x_o	-1.0 KPa
a	3.86 KPa
θ	0.21
D	1.2E-6 Pa^{-1}
W	0.01

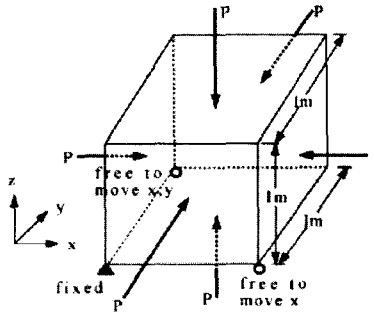

(a) Single element mesh for hydrostatic loading set

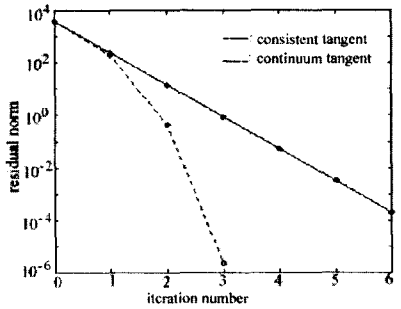

(b) Finite element force convergence characteristics of the model

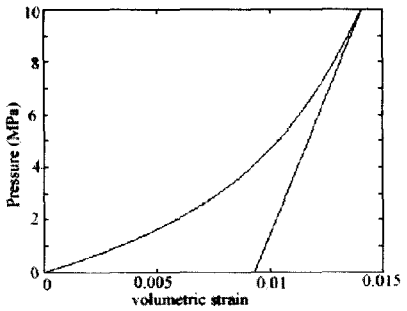

(c) Pressure vs. volumetric strain response of the material model

Fig. 1 Hydrostatic compression test

model. A single finite element in Fig. 1a is subjected to a stress-controlled hydrostatic loading test, and the strain response of the element is computed and displayed in Fig. 1b. To demonstrate the rate of convergence achieved with the consistent tangent operator expressions provided in the previous section, the convergence behavior for a single load-step during this test is shown in Fig. 1c, and shows an asymtotically quadratic rate of convertgence. The cap model material parameters used in this test are listed in Table 4.

4.2 Four Element Limit Analysis Computation

While the preceding model demonstrated the performance of the model under purely hydrostatic loading, this simple four element test is designed to show the model's performance under combined deviatric and compressive loading. In this test computation, the loading shown on the four element mesh (Fig. 2a) is increased until the limit state of the model is found using methods obtained in Swan and Seo(1999). The computed load-displacement response of the model is shown in Fig. 2b, and the material model parameters utilized are listed below in Table 6. In this test which involved plastic loading at the crown of the cap at limit state, very good convergence behavior was achieved.

4.3 Slope Stability Analysis Computations

In these computations, an earthen slope model comprised

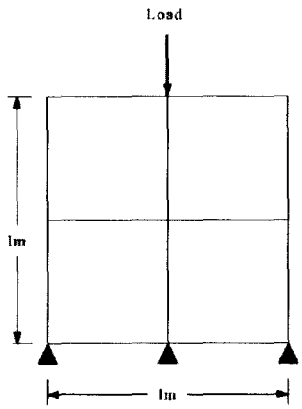

(a) Simple plane strain four element mesh with applied loading and restrains

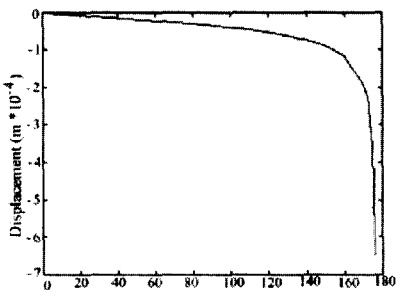

(b) The computed load-deformation response provided by the smooth cap model

Fig. 2 Four element limit analysis computation

Table 5. Material parameters used in four element limit analysis test

Material Parameter	value
μ	208.3 MPa
E	500.0 MPa
x_o	-100.0 kPa
α	12.3 kPa
θ	0.2003
D	3.2E-7 Pa^{-1}
W	0.15

Table 6. Sand-like material parameters used in slope stability analysis

Parameter	Value(Loose Sand)	Value(Dense Sand)
ρ	1800 kg/m^3	1800 kg/m^3
μ	1.2 GPa	1.2 GPa
E	3.0 GPa	3.0 GPa
x_o	-500.0 KPa	-1.0 kPa
α	30.0 Pa	30.0 Pa
θ	0.2	0.2
D	3.2E-8 Pa^{-1}	3.2E-8 Pa^{-1}
W	0.07	0.07

of a sandy soil is analyzed for stability using the methods proposed in Swan and Seo(1999), which involved increasing the gravitational loading on the slope model until a failure mechanism develops, and the slope model can take no further loading. The mesh used to model the slope is shown in Fig. 3 and contains 1130 bilinear continuum plane strain finite elements. The finite slope shown has a height of 30m and a response angle of 29.98° . For a loose sandy soil and dense sandy soil whose parameters are shown in Table 6, the computed stability factors of safety for this model were 0.95 and 0.98, respectively.

5. Summary and Closure

A smooth, three-surface cap model has been presented here along with sample computations which demonstrate its very good performance characteristics. The model retains many of the positive physical attributes of preceding non-smooth cap models, but avoids many of the numerical difficulties associated with corner points in those models: the numerical integration algorithms and consistent tangent operator expressions. The rate of convergence achieved in the sample implicit finite element computations presented was typically asymptotically quadratic.

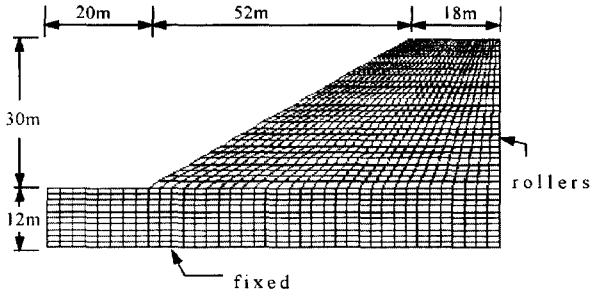

Fig. 3 Mesh of 1130 bilinear continuum plane-strain finite elements used in slope stability analysis

Elasto-plastic cap models of the type presented here are quite useful in modeling ductile soil behaviors. To capture softening behaviors in porous media which are also of considerable interest, cap models such as this one can be straightforwardly coupled with continuum damage mechanics models.

References

1. DiMaggio, F. L. and Sandler, I. S. (1971), "Material models for granlur soils", J. of Eng. Mech., ASCE, Vol 97. No. EM3 June pp. 935-950.
2. Hofstetter, G., Simo, J. C. and Taylor, R. L. (1993) "A modified cap model: closest point solution algorithms", Computers & Structures, 48-2, pp. 203-214.
3. Simo, J. C. and Taylor, R. L. (1985) "Consistent tangent operators for rate-independent elastoplasticity", Comp. Meth. Appl. Mech. Eng., 48, pp. 101-118.
4. Swan, C. C. and Seo, Y-K (1999), "Limit atate analysis of earthern slopes using a continuum/FEM approach", Int. J. Numer. Analy. Methods in Geomech., 23, pp. 1359-1371.

(received on Mar. 22, 2001)